



## Magnetic resonance imaging of reconstructed ferritin as an iron-induced pathological model system



Lucia Balejčiková<sup>a,b</sup>, Oliver Strbak<sup>b,c</sup>, Ladislav Baciak<sup>d</sup>, Jozef Kováč<sup>a</sup>, Marta Masarova<sup>b</sup>, Andrej Krafcik<sup>b,\*</sup>, Ivan Frollo<sup>b</sup>, Dusan Dobrota<sup>c</sup>, Peter Kopčanský<sup>a</sup>

<sup>a</sup> Institute of Experimental Physics SAS, Watsonova 47, 040 01 Kosice, Slovakia

<sup>b</sup> Institute of Measurement Science SAS, Dubravska cesta 9, 841 04 Bratislava 4, Slovakia

<sup>c</sup> Biomedical Center Martin, Jessenius Faculty of Medicine in Martin, Comenius University in Bratislava, Mala Hora 4, 036 01 Martin, Slovakia

<sup>d</sup> Faculty of Chemical and Food Technology STU, Radlinskeho 9, 812 37 Bratislava, Slovakia

### ARTICLE INFO

#### Keywords:

Ferritin  
Reconstructed ferritin  
Iron overloading  
Dynamic light scattering  
SQUID magnetometry  
Magnetic resonance imaging

### ABSTRACT

Iron, an essential element of the human body, is a significant risk factor, particularly in the case of its concentration increasing above the specific limit. Therefore, iron is stored in the non-toxic form of the globular protein, ferritin, consisting of an apoferritin shell and iron core. Numerous studies confirmed the disruption of homeostasis and accumulation of iron in patients with various diseases (e.g. cancer, cardiovascular or neurological conditions), which is closely related to ferritin metabolism. Such iron imbalance enables the use of magnetic resonance imaging (MRI) as a sensitive technique for the detection of iron-based aggregates through changes in the relaxation times, followed by the change in the inherent image contrast. For our *in vitro* study, modified ferritins with different iron loadings were prepared by chemical reconstruction of the iron core in an apoferritin shell as pathological model systems. The magnetic properties of samples were studied using SQUID magnetometry, while the size distribution was detected via dynamic light scattering. We have shown that MRI could represent the most advantageous method for distinguishing native ferritin from reconstructed ferritin which, after future standardisation, could then be suitable for the diagnostics of diseases associated with iron accumulation.

### 1. Introduction

Ferritin, the iron storage biomacromolecule, consists of a hollow spheroidal shell, apoferritin, which is 12 nm in diameter and formed by 24 protein subunits joined by non-covalent bonds arranged in 4,3,2 symmetry. Ferritin is composed of two functionally and genetically different types of protein subunits H- and L- [1], which are marked according to their molecular weight: H- Heavy subunit ~ 21 kDa, and L- Light subunit ~ 19 kDa [2]. H-subunits have a natural ferroxidase function for rapid Fe<sup>2+</sup> oxidation and iron loading into apoferritin. Meanwhile, L-subunits are responsible for the mineralisation of iron atoms in apoferritin, followed by ferritin formation [3]. The distribution ratio of the H-/L- subunits is tissue-specific [4]. The majority of the H-subunits are in the heart and brain, which are exposed to a high degree of oxidation activity and a predominance of L-subunits, as in the liver, which functions primarily as a storage facility. On the ferritin surface, two types of protein channels are situated with an average ~ 0.4 nm. The role of the 8×3-fold hydrophilic, polar and negatively

charged channels is the capture and release of ferrous ions. The electron transfer is mediated through the 6×4-fold hydrophobic, nonpolar channels [5]. The molecular weight of ferritin is ~ 450 kDa, depending on the organ or organism from which the ferritin was isolated [6]. Physiological ferritin has the ability to store up to 4500 iron atoms, arranged in a crystal lattice bearing similarity to ferrihydrite mineral [3]. In a healthy human body, the stored iron is then gradually released from ferritin as Fe<sup>2+</sup> ions according to the specific bodily requirements (e.g. pregnancy, haemorrhage, iron deficiency in diet, etc.) [7,8], regulated in particular by an autocatalytic function of ferritin [3].

It is quite well known that many diseases (e.g. cancer, cardiovascular or neurological conditions) are associated with iron homeostasis disorders, which are closely related to ferritin metabolism [9–11]. The accumulation of dangerous iron ions could create free radicals via Fenton and Haber-Weiss reactions [12], and thus damage the structure and storage function of ferritin [13,14]. The result is the onset of a range of pathological chain reactions, damaging cells, tissues and

Abbreviations: DLS, dynamic light scattering; GE, gradient echo; LF, loading factor; MEMS, multi echo multi slice; NA, native apoferritin; NF, native ferritin; PDI, polydispersity index; RF, reconstructed ferritin; MGEMS, multi gradient echo multi slice; STIR, short TI, inversion recovery; TSE, turbo spin echo

\* Corresponding author.

<http://dx.doi.org/10.1016/j.jmmm.2016.11.019>

Received 25 June 2016; Received in revised form 19 October 2016; Accepted 1 November 2016

Available online 05 November 2016

0304-8853/ © 2016 Elsevier B.V. All rights reserved.

organs, and which could ultimately lead to the death of the organism [9,15]. Early diagnosis of such iron-induced disorders can assist in correcting such pathological events, slowing their progress, reducing the harmful factors and aiding in the selection of a suitable medical procedure to halt the process. Such diagnostic method could be MRI, which is sensitive to iron agglomeration detection through the modification of the MRI signal. In many studies, MRI was successfully applied to allow the detection of iron in chemically or genetically modified ferritin [16–18]. Inspired by previous works, we have focused on the MRI of chemically modified RFs with different iron loadings as a pathological model system of iron overloading as a result of disrupted iron homeostasis. *In vitro* reconstruction of ferritin was mentioned in many studies, oriented towards the understanding of ferritin kinetics, its autocatalytic function and the mechanisms of iron ions' uptake. Such RF should consist of apoferritin, which surrounds a synthetically prepared iron core [19–21].

In the present work, the MRI enables the detection and discrimination between NF and RF aqueous solutions. In addition, the studied solutions were dispersed in a gelatine medium that represented the *in vitro* model of brain tissue. SQUID magnetometry up to 5 T was employed to obtain the magnetisation data. The size distribution and colloidal stability were verified by DLS. Our study has demonstrated that RF, containing various amounts of iron, could be a useful MRI standard in applied research for the diagnostics of various diseases associated with iron overloading in pathological tissue [22–24].

## 2. Materials and methods

### 2.1. Chemicals

Ammonium ferrous sulphate hexahydrate ((NH<sub>4</sub>)<sub>2</sub>Fe(SO<sub>4</sub>)<sub>2</sub>·6H<sub>2</sub>O), equine spleen apoferritin in 0.15 M NaCl, ethanol (C<sub>2</sub>H<sub>6</sub>O), horse spleen ferritin in 0.15 M NaCl, hydrogen peroxide (H<sub>2</sub>O<sub>2</sub>), 4-(2-hydroxyethyl)-1-piperazineethanesulfonic acid (HEPES), sodium hydroxide (NaOH), and trimethylamine N-oxide (Me<sub>3</sub>NO) were obtained from SIGMA-Aldrich; Coomassie brilliant blue from Fluka; hydrochloric acid (HCl) from ITES; potassium thiocyanate (KSCN) from Slavus; and phosphoric acid (H<sub>3</sub>PO<sub>4</sub>) from Centralchem, while food gelatine and demineralised were sourced locally.

### 2.2. Synthesis of reconstructed ferritin

RF was prepared by gradual additions of ferrous ions into the empty protein shell of NA. First, the pH of 0.02 M HEPES buffer was adjusted by 2 M NaOH solution to a final value 7.4, which was controlled by utilising a pH meter (Mettler Toledo SevenEasy S20-KS) and pH electrode (Mettler Toledo Inlab®Science Pro). Demineralised water, used for the preparation of all the solutions, was deaerated using inert nitrogen for ~ 1 h to ensure anaerobic conditions and the controlled oxidation of ferrous ions. Apoferritin solution was diluted in a HEPES buffer to obtain the final concentration of ~ 3 mg/mL, with the reaction bottle then hermetically enclosed. Ferrous ions as 0.1 M solution of Mohr's salt ((NH<sub>4</sub>)<sub>2</sub>Fe(SO<sub>4</sub>)<sub>2</sub>·6H<sub>2</sub>O) and oxidant as a 0.07 M solution of trimethylamine N-oxide were added into the reaction solution in a stoichiometric ratio 3:2 ten times over 100 min using syringes at 37 °C under constant stirring in a magnetic stirrer with heating (IKA C-MAG HS 7). Several sample types with different LFs, representing the average number of iron atoms per one apoferritin biomacromolecule, were prepared. For comparison with aqueous solutions, a gelatine medium was prepared by dissolving gelatine powder in a HEPES buffer. The samples were diluted 1:100 and dispersed in a warm gelatine medium before solidification.

### 2.3. Quantitative determination of loading factor

Quantitative determination of LF was performed using a UV–vis

spectrophotometer (SPECORD 40, Analytik Jena) at 25 °C with a precision of approximately 1%. The mass concentration of iron atoms  $c_m^{Fe}$  was obtained following oxidation of Fe<sup>2+</sup> to Fe<sup>3+</sup> ions with 3% H<sub>2</sub>O<sub>2</sub> in an acid medium of concentrated 35% HCl at 50 °C for 30 min. The product of the Fe<sup>3+</sup> ions with 1 M KSCN reaction was a red thiocyanate complex of Fe[Fe(SCN)<sub>6</sub>], with its absorbance measured at the wavelength of the light, namely 450 nm. The mass concentration of iron atoms was calculated utilising the regression equation from the linear calibration curve. The mass concentration of NA,  $c_m^{NA}$ , was obtained using the standard Bradford method. The absorbance of blue coloured complex of Bradford agent with protein residues was detected at the wavelength of the light (595 nm) after 5 min incubation at 25 °C. From the calculated ratio of  $c_m^{Fe}$  and  $c_m^{NA}$  in a given volume of sample employing the known molecular weights of NA and iron, respectively, the LF of the RFs was calculated according to the equation:

$$LF = \frac{c_m^{Fe} \cdot M_{NA}}{c_m^{NA} \cdot M_{Fe}} \quad (1)$$

### 2.4. Measurement of hydrodynamic diameter

The hydrodynamic diameter of ferritin and RF colloidal solutions in 0.02 M HEPES buffer with pH 7.4 was measured by Zetasizer NanoZS 3600 (Malvern Instruments) utilising DLS, also referred to as photon correlation spectroscopy or quasi-elastic light scattering.

The average hydrodynamic diameter  $\langle D_{HYDR} \rangle$  was measured in triplicate using disposable polystyrene cuvettes in the protein data analysis mode at 25 °C. The size distribution was displayed in the Zetasizer software as a dependence of the relative number of particles on their size, where the average diameter represented the maximum of the curve.

The next specific DLS parameter is the PDI, which represents a number (in the range from 0 to 1), where the maximum value (1) indicates that the sample has a very broad size distribution and may contain large particles or aggregates with sedimentation tendency [25].

### 2.5. Magnetometry

The magnetic properties of the samples in liquid medium were studied using a SQUID magnetometer (Quantum Design MPMS 5XL), with the hysteresis loops on the prepared samples measured with the assistance of this equipment at a temperature of 290 K in the range of the induction of the magnetic field up to 5 T.

### 2.6. MRI

MRI measurements were performed at low-field 0.2 T ESAOTE system, as well as at high-field 4.7 T VARIAN system. With both systems, the relative contrast of the ferritin samples (NF, RF, and MF in comparison with apoferritin) was measured and analysed. Standard T<sub>2</sub>-weighted protocols were utilised for the ferritin imaging.

Low-field system:

- GE pulse sequence with a repetition time TR=600 ms, and an echo time TE=22 ms
- STIR pulse sequence with TR=1960 ms, and TE=80–120 ms
- TSE pulse sequence with TR=3000 ms, and TE=80–120 ms

High-field system:

- MEMS pulse sequence, with TR=2000 ms, commencing echo time TE=10 ms, followed by 16 gradually increased times (20, ..., 160)
- MGEMS pulse sequence, with TR=105 ms, and commencing echo time TE=6 ms, followed by 16 gradually increased times

The relative contrast is defined as follows:

$$RC = (I - I_0)/I_0 \quad (2)$$

where  $I_0$  is the signal intensity without magnetite nanoparticles, and  $I$  represents the signal intensity with magnetite nanoparticles.

The interpolated value of NF's relative contrast in the RF curve ( $RC_{interp}^{NF}$ ) was determined, and then the final difference in the relative contrast ( $RC_{diff}$ ) of the interpolated NF and NF was evaluated (Fig. 9a,b):

$$RC_{diff} = |RC_{interp}^{NF} - RC^{NF}|$$

Moreover, the transversal relaxation time  $T_2$  of all the ferritin samples was obtained spectroscopically through the Car-Purcell-Meiboom-Gill echo pulse sequence at the high-field system. Consecutively, the transversal relaxation rate  $R_2$  and relaxivity were determined for the RF and MF samples. The transversal relaxation rate  $R_2$  is inverse to the transversal relaxation time  $T_2$ , with the transverse relaxivity  $r_2$  calculated as follows:

$$r_2 = (R_2 - R_2^0)/C \quad (3)$$

where  $R_2^0$  is the transverse relaxation rate in the absence of nanoparticles,  $R_2$  represents the transverse relaxation rate in the presence of nanoparticles, and  $C$  is the nanoparticles' concentration. For image data processing and MRI parameter analysis we employed the following software tools: Marevisi (NRC - Institute for Biodiagnostic, Winnipeg, Canada), and Matlab R2011b (Mathworks Inc., Natic, USA).

### 3. Results and discussion

Initially, RFs with various LFs (424, 913, 1771, 2396, 3926 and 4790) were prepared. The proper LF for iron-containing samples was determined using UV–vis spectrophotometry with an error less than 2% (Table 1). RFs, NA and ferritin as reference solutions were then diluted in HEPES buffer and gelatine medium, respectively, for comparative MRI studies.

The average hydrodynamic diameter,  $\langle D_{HYDR} \rangle$ , of apoferritin, ferritin and RFs in aqueous solutions was obtained by DLS (Tab. 1). The  $\langle D_{HYDR} \rangle$  provides information regarding the effective size of the hydrated/solvated particles and is dependent upon both the mass and shape (conformation); therefore, it could be larger than the particles size determined using other methods such as transmission electron microscopy. The determined  $\langle D_{HYDR} \rangle$  depended on the LF and achieved the detection limit for the RFs with the LFs 2396, 3926 and 4790 (Tab. 1), which cannot be measured with the Malvern Nano ZS 3600. The PDIs of samples, collected in Tab. 1, correlated with the  $\langle D_{HYDR} \rangle$  and are pointed out the highly polydisperse samples. Samples with LFs 2396, 3926 and 4790 achieved the maximum PDI, which was observed as visible sedimentation after several minutes. These samples were suitable to represent a model situation of pathological iron accumulation.

For better simulation of the iron deposits formed during Alzheimer's disease, created aggregates were fixed in a gelatine

**Table 1**

Basic parameters obtained from UV–vis quantitative analysis and DLS measurements.

Sample	LF	$\langle D_{HYDR} \rangle$ [nm]	PDI
NA HEPES	0	14.81	0.636
NF HEPES	884	18.66	0.284
RF	424	15.51	0.0503
RF	913	103.1	0.417
RF	1771	226.2	0.599
RF	2396	> 10 $\mu\text{m}$	1.000
RF	3926	> 10 $\mu\text{m}$	1.000
RF	4790	> 10 $\mu\text{m}$	1.000

medium that represented the *in vitro* model of brain tissue (Fig. 1).

The magnetisation curves of NF and RFs at different LFs did not show hysteresis at a temperature of 295 K, which is typical superparamagnetic behaviour for a system containing small nanoparticles (Fig. 2). The magnetisation data were normalised to the total mass of the sample. The magnetisation behaviour does not increase linearly with the LF of RF, which could be associated with various types of iron-phase formation. Unfortunately, the magnetisation was unable to offer any information regarding the precise iron composition of the inorganic part of the samples. Therefore, future work should conduct detailed X-ray powder diffraction study following the separation of the secondary products of synthesis for potential bio-applications. No saturation magnetisation was observed for the samples, implying superparamagnetic behaviour of the small nanoparticles. We assumed the presence of iron hydroxides or iron oxide-hydroxides in the samples. The unspecific formation of these substances outside of the protein shell as a consequence of the unknown reaction kinetics is not excluded. Furthermore, the physico-chemical conditions of the synthesis could not be precisely controlled due to the hermetically enclosed reaction bottle; therefore, we could not monitor the reaction intermediates, pH or pressure changes, for example. Ubiquitous oxygen also complicates the controlled synthesis. As it is visible from the field dependencies of magnetisation, all samples excluding NF contain a significant part of material with diamagnetic properties, which subsequently deforms the shape of the field dependences of magnetisation, in spite of our efforts to subtract the expected contributions from the NA and samples capsule. There probably exists internal components of molecules connected with the ions of Fe which are causing this diamagnetic signal. Our investigations using DLS and SQUID magnetometry could not clearly distinguish between the iron-based aggregates formed inside or outside of the protein. The detailed study of these aggregates could help enhance our understanding of the role of ferritin, iron and its compounds in the development of diseases. However, in our case we would like to point out that our work is targeted towards the MRI scanning of iron-based aggregates, which helps us to simulate pathological events.

Subsequently, NF and RF were analysed using MRI techniques, both in low-field (0.2 T ESAOTE) and high-field (4.7 T Varian) systems. Figs. 3–5 present the relative contrast of RF in buffer, as well as in gelatine, measured at 0.2 T, with three different T2 weighted sequences: GE (Fig. 3), STIR (Fig. 4) and TSE (Fig. 5). In all three buffer cases (blue line), the NF is clearly distinguishable from the RF. Although the relative contrast value  $RC_{diff}$  is maximal for the TSE sequence ( $\approx 30\%$  for TE=110 ms), the most optimal sequence for RF in buffer seems to be STIR, particularly with echo time TE=110 ms ( $RC_{diff} \approx 20\%$ ). This is due to the STIR pulse sequence having no data inconsistency in a curve shape for different echo times (unpublished results) like TSE, and demonstrates the bigger difference in  $RC_{diff}$  value ( $\approx 20\%$ ), in comparison with the GE pulse sequence ( $\approx 15\%$ ).

After fixation of the samples in gelatine (cyan line), we can see the slightly modified trend in the curved shape. The difference between the NF and its interpolated value tends to be a little smaller (Fig. 8), with the relative contrast differences of the RF for different LFs being almost smooth. In the case of the STIR protocol (Fig. 4), the RC of the RF is lower for all the LFs than for the NF, which is in contrast with the buffer data, and our experience. The real reason for this is unknown, but possible alternatives are discussed below. To conclude, Figs. 3–5 compare the samples with and without fixation into gelatine, measured at 0.2 T for the following pulse sequences: GE, STIR, and TSE. The smoothing effect of the fixation of samples into gelatine is clearly visible. In the case of the GE protocol (Fig. 3), the RC values of the RF, as well as that of the NF, are very similar for almost all the LFs. For the STIR pulse sequence (Fig. 4), the situation is highly comparable, except for the NF parameter, which changes in the opposite way. In the TSE protocol, the differences are significantly larger, but only for the RF with higher LF (Fig. 5). The NF values are again, as for the GE, almost



Fig. 1. A photo of samples in gelatine: (from the left) pure gelatine, NA, NF, RF with LFs 424, 913, 1771, 2396, 3926 and 4790.

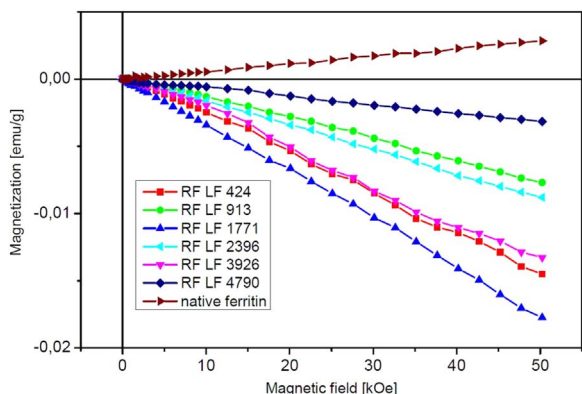


Fig. 2. Magnetisation: field dependencies of the RFs with LFs in the 424–4790 range.

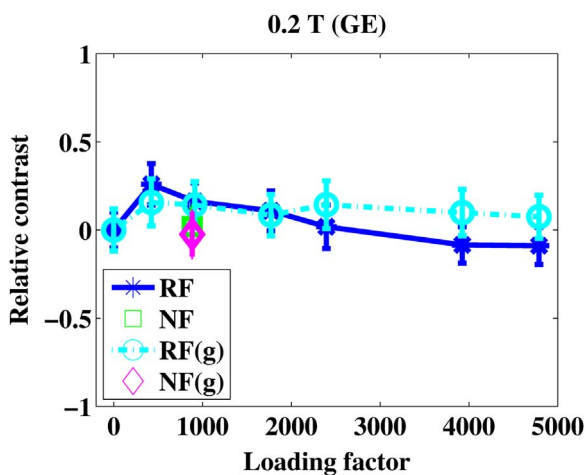


Fig. 3. Comparison of the relative contrast of NF and RF in buffer and gelatine (g), with different LFs. Samples were measured at 0.2 T with GE pulse sequence (TR=600 ms, TE=22 ms). (For interpretation of the references to color in this figure, the reader is referred to the web version of this article.).

identical.

A very similar trend can also be seen in the results measured at 4.7 T with the MEMS (Fig. 6) and MGEMS (Fig. 7) protocols, although the differences between the RC of the NF and its interpolated value are not particularly large. The smoothing trend of the fixation of samples into gelatine is also very obvious for both pulse sequences (cyan lines). The  $RC_{diff}$  value is almost equal to zero for the samples in gelatine (Fig. 9). In comparison, the  $RC_{diff}$  value is around 15–20% in the samples without gelatine (Fig. 9).

In conclusion, we can say that the fixation of the ferritin particles into gelatine, and increasing the used MRI field, decreases the possibility of differentiating the NF (as a physiological model system) from the RF (as a pathological model system). This is probably caused by the fact that during high-field image acquisition, the larger amount of proton magnetic moments is involved in final signal creation,

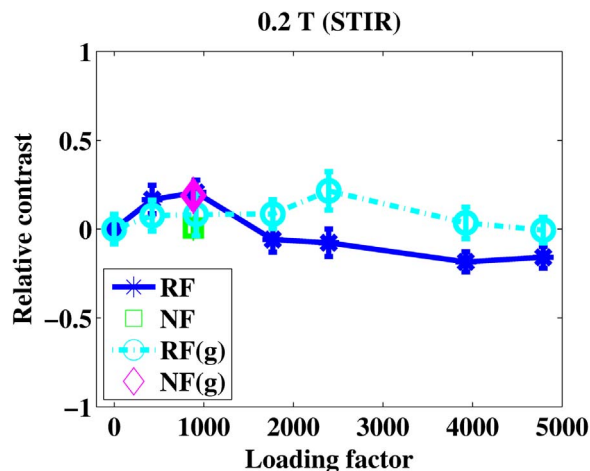


Fig. 4. Comparison of the relative contrast of NF and RF in buffer and gelatine (g), with different LFs measured at 0.2 T and the STIR pulse sequence (TR=1960 ms, TE=110 ms).

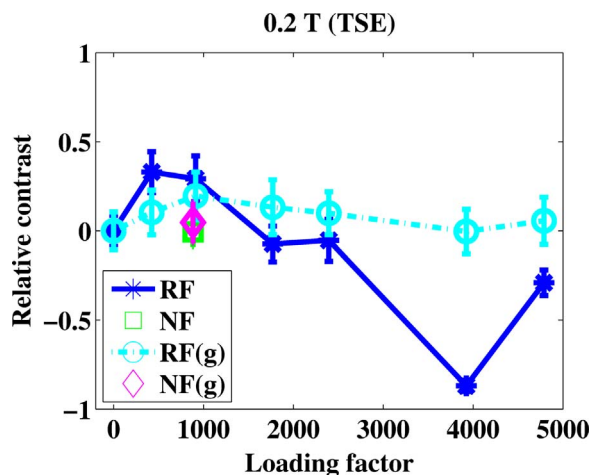


Fig. 5. Comparison of the relative contrast of NF and RF in buffer and gelatine (g), with different LFs measured at 0.2 T and the TSE pulse sequence (TR=3000 ms, TE=110 ms).

averaging such inhomogeneities caused by the iron oxides in the RF. We also assume that all variations in the RC of the samples with and without gelatine are caused by incomplete homogeneous entrapping of the ferritin particles in the gelatine matrix, during the solidification process (Fig. 1). The subsequent slice selection during MRI in such non-homogeneous regions results in mild changes in the RC of the samples with and without gelatine. Such variation could probably be solved by the selection of thicker slices during the slice selection process (we utilised a slice thickness of 3 mm). Smoothing of the gelatine-entrapped data suggests the turbulent dynamics of the ferritin particles in the homogenised buffer solutions. Such dynamic behaviour is prevented after the fixation of the samples into gelatine. It is necessary to consider such error of liquid samples, particularly in the

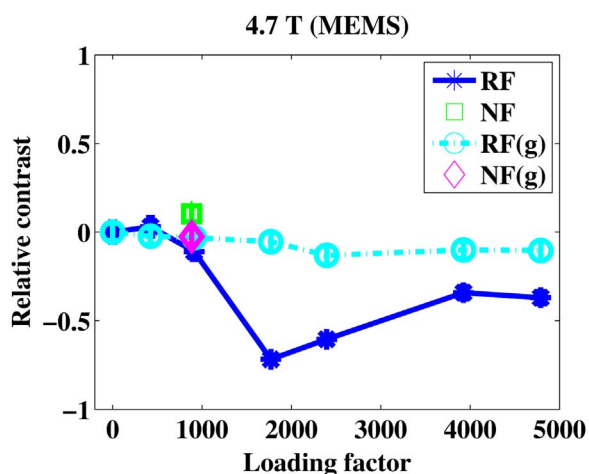


Fig. 6. Comparison of the relative contrast of NF and RF in buffer and gelatine (g), with different LFs measured at 4.7 T and the MEMS pulse sequence (TR=2000 ms).

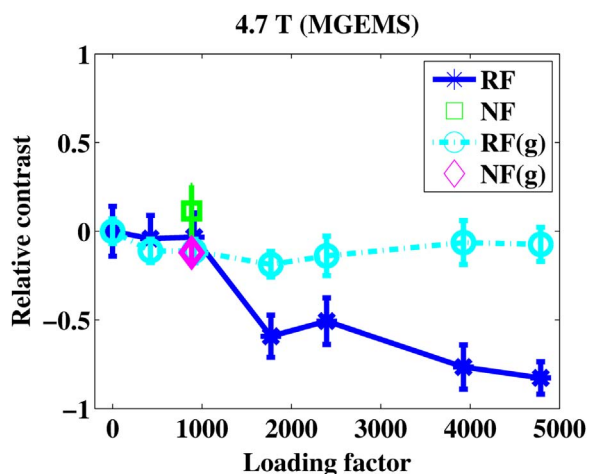


Fig. 7. Comparison of the relative contrast of NF and RF in buffer and gelatine (g), with different LFs measured at 4.7 T and the MGEMS pulse sequence (TR=105 ms).

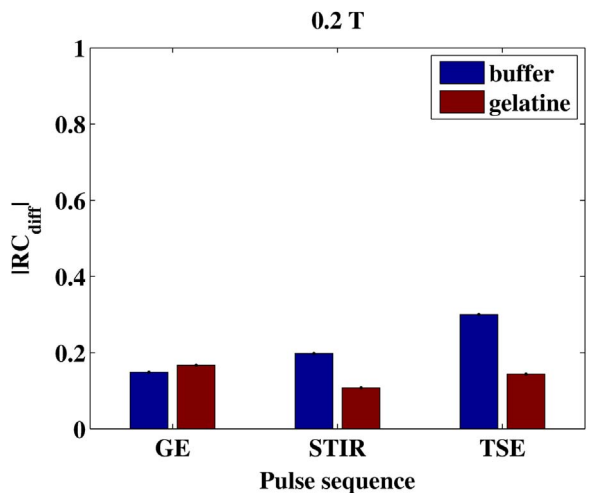


Fig. 8. Difference in relative contrast value ( $RC_{diff}$ ) of interpolated NF and NF, for different pulse sequences measured at 0.2 T.

case of calibration samples prepared for ferritin quantification *in vivo*, where the ferritin particles are statically entrapped in the brain tissue. In Fig. 10 we can also see the smoothing effect of fixation in the case of  $T_2$  relaxation time.

Apart from this, we can conclude that all the used T2-weighted

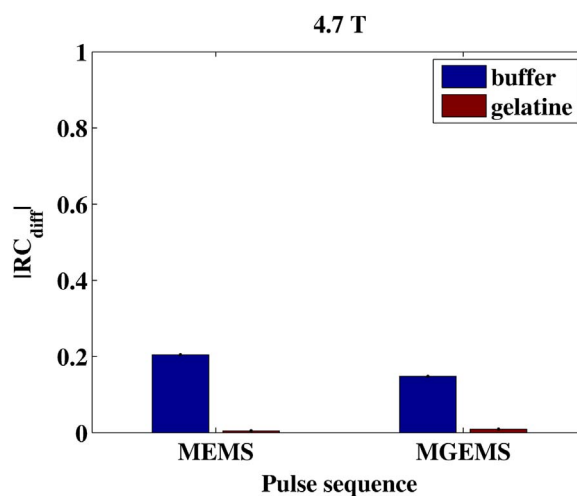


Fig. 9. Difference in relative contrast value ( $RC_{diff}$ ) of interpolated NF and NF, for different pulse sequences measured at 4.7 T.

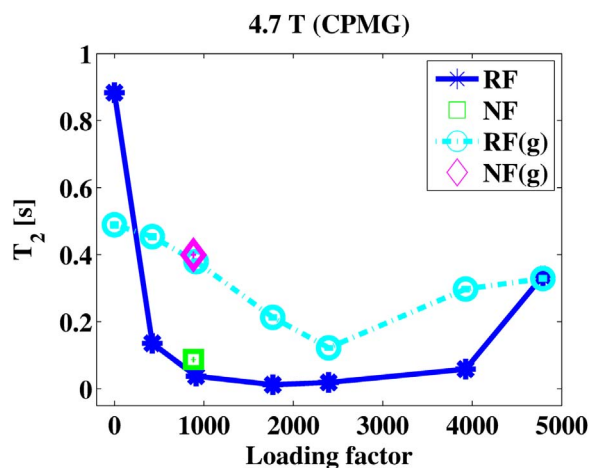


Fig. 10. The transversal relaxation time  $T_2$  of RF and NF in buffer and gelatine, obtained spectroscopically through the Car-Purcell-Meiboom-Gill echo pulse sequence at 4.7 T.

pulse sequences at low-field (GE, STIR, TSE), as well as in the high-field (MEMS, MGEMS) system are suitable for ferritin contrast imaging. However, in order to achieve the best contrast to differentiate NF as a physiological model system, from RF as a pathological model system, we suggest measuring the calibration samples in buffer, at low-field with standard  $T_2$ -weighted protocols. In the case of *in vivo* quantification, the calibration samples should be fixed (e.g. in gelatine) to avoid the above-mentioned dynamics error and as such to facilitate the differentiation of inhomogeneities caused only by accumulated iron.

#### 4. Conclusion

Our work presented the results of a comparative study of NF and RF with different LFs by combination of DLS, SQUID magnetometry and MRI measurement. The DLS data have shown the change of average hydrodynamic diameter and an increasing polydispersity with the LF growth. The magnetisation data without hysteresis at 290 K were not linearly dependent on the LF, which contributed to the presence of free iron ions in the studied systems. The differences in MRI contrast allowed discrimination between NF and RF in liquid (buffer) and solid (gelatine) medium. After future standardisation, MRI could become a suitable method that is sufficiently sensitive for the diagnosis of diseases associated with iron overloading and aggregation.

## Acknowledgements

This work was supported by the Slovak Research and Development Agency project no. APVV-0431-12, by the Slovak Scientific Grant Agency VEGA (projects no. 2/0045/13, 2/0013/14, and 1/0377/16), by the Ministry of Education's Agency for European Structural Funds (projects no. 26220120021 and 26220220186), and CENTER OF EXCELLENCE FOR RESEARCH IN PERSONALIZED THERAPY (CEVYPET, co-funded from the EU sources and European Regional Development Fund, ITMS: 26220120053).

## References

- [1] E.C. Theil, H. Takagi, G.W. Small, L. He, A.R. Tipton, D. Danger, *Inorg. Chim. Acta* 297 (2000) 242.
- [2] D. Finazzi, P. Arosio, *Arch. Toxicol.* 88 (2014) 1787.
- [3] N.D. Chasteen, P.M. Harrison, *J. Struct. Biol.* 126 (1999) 182.
- [4] P.M. Harrison, P. Arosio, *Biochim. Biophys. Acta* 1275 (1996) 161.
- [5] R.K. Watt, R.J. Hilton, D.M. Graff, *Biochim. Biophys. Acta* 1800 (2010) 745.
- [6] M. Wagstaff, M. Worwood, A. Jacobs, *Biochem. J.* 173 (1978) 969.
- [7] Y. Ren, T. Walczyk, *Metallomics* 6 (2014) 1709.
- [8] Y.-H. Pan, K. Sader, J.J. Powell, A. Bleloch, M. Gass, J. Trinick, A. Warley, A. Li, R. Brydson, A. Brown, *J. Struct. Biol.* 166 (2009) 22.
- [9] A. Friedman, P. Arosio, D. Finazzi, D. Kozirowski, J. Galazka-Friedman, *Parkinsonism Relat. Disord.* 17 (2011) 423.
- [10] M.J. Williams, R. Poulton, S. Williams, *Atherosclerosis* 165 (2002) 179.
- [11] A.A. Alkhateeb, J.R. Connor, *Biochim. Biophys. Acta* 1836 (2013) 245.
- [12] S. Chen, P. Schopfer, *Eur. J. Biochem.* 260 (1999) 726.
- [13] C. Quintana, M. Lancin, C. Marhic, M. Pérez, J. Martin-Benito, J. Avila, J.L. Carrascosa, *Cell. Mol. Biol.* 46 (2000) 807.
- [14] C. Quintana, J.M. Cowley, C. Marhic, *J. Struct. Biol.* 147 (2004) 166.
- [15] X. Huang, *Mutat. Res.* 533 (2003) 153.
- [16] X. He, J. Cai, B. Liu, Y. Zhong, Y. Qin, *Stem Cell. Res. Ther.* 31 (2015) 207.
- [17] L. Liu, K. Gong, P. Ming, Y. Huang, Q. Tang, G. Xu, J. Yan, N. Zhao, X. Zhang, Y. Gong, *Biotechnol. Lett.* 32 (2010) 743.
- [18] B. Iordanova, T.K. Hitchens, C.S. Robison, E.T. Ahrens, *PLoS One* (8) (2013) e72720.
- [19] I.G. Macara, T.G. Hoy, P.M. Harrison, *Biochem. J.* 126 (1972) 151.
- [20] S. Levi, A. Luzzago, G. Cesareni, A. Cozzi, F. Franceschinelli, A. Albertini, P. Arosio, *J. Biol. Chem.* 263 (1988) 18086.
- [21] S. Sun, N.D. Chasteen, *J. Biol. Chem.* 267 (1992) 25160.
- [22] Q. Pankhurst, D. Hautot, K. Nadeem, J. Dobson, *J. Alzheimers Dis.* 13 (2008) 49.
- [23] J.M. Graham, M.N.J. Paley, R.A. Grunewald, N. Hoggard, P.D. Griffiths, *Brain* 123 (2000) 2423.
- [24] W. Beyhum, D. Hautot, J. Dobson, Q.A. Pankhurst, *J. Phys. Conf. Ser.* 17 (2005) 50.
- [25] Nano Zetasizer, Series: User Manual, Malvern Instruments Ltd., United Kingdom, 2007, p. 292.